Title
First light of the Gemini Planet Imager

Journal
Proceedings of the National Academy of Sciences of the United States of America, 111(35)

ISSN
0027-8424

Authors
Macintosh, Bruce
Graham, James R
Ingraham, Patrick
et al.

Publication Date
2014-09-02

DOI
10.1073/pnas.1304215111

Peer reviewed

SPECIAL FEATURE

First light of the Gemini Planet Imager

Bruce Macintosh[a,b,1], James R. Graham[c], Patrick Ingraham[b], Quinn Konopacky[d], Christian Marois[e], Marshall Perrin[f], Lisa Poyneer[a], Brian Bauman[a], Travis Barman[g], Adam S. Burrows[h], Andrew Cardwell[i], Jeffrey Chilcote[j], Robert J. De Rosa[k], Daren Dillon[l], Rene Doyon[m], Jennifer Dunn[e], Darren Erikson[e], Michael P. Fitzgerald[j], Donald Gavel[l], Stephen Goodsell[i], Markus Hartung[i], Pascale Hibon[i], Paul Kalas[c], James Larkin[j], Jerome Maire[d], Franck Marchis[n], Mark S. Marley[o], James McBride[c], Max Millar-Blanchaer[d], Katie Morzinski[p], Andrew Norton[l], B. R. Oppenheimer[q], David Palmer[a], Jennifer Patience[k], Laurent Pueyo[f], Fredrik Rantakyro[i], Naru Sadakuni[i], Leslie Saddlemyer[e], Dmitry Savransky[r], Andrew Serio[i], Remi Soummer[f], Anand Sivaramakrishnan[f,q], Inseok Song[s], Sandrine Thomas[o], J. Kent Wallace[t], Sloane Wiktorowicz[l], and Schuyler Wolff[u]

[a]Lawrence Livermore National Laboratory, Livermore, CA 94551; [b]Kavli Institute for Particle Astrophysics and Cosmology, Stanford University, Stanford, CA 94305; [c]Astronomy Department, University of California, Berkeley, CA 94720; [d]Dunlap Institute for Astronomy and Astrophysics, University of Toronto, Toronto, ON, Canada M5S 3H4; [e]National Research Council of Canada Herzberg, Victoria, BC, Canada V9E 2E7; [f]Space Telescope Science Institute, Baltimore, MD 21218; [g]Lunar and Planetary Laboratory, University of Arizona, Tucson, AZ 85721; [h]Department of Astrophysical Sciences, Princeton University, Princeton, NJ 08544; [i]Gemini Observatory, Hilo, HI 96720; [j]Department of Physics and Astronomy, University of California, Los Angeles, CA 90095; [k]School of Earth and Space Exploration, Arizona State University, Tempe, AZ 85287; [l]University of California Observatories/Lick Observatory, University of California, Santa Cruz, CA 95064; [m]Observatoire du Mont-Mégantic and Département de Physique, Université de Montréal, Montréal, QC, Canada H3T 1J4; [n]SETI Institute, Carl Sagan Center, Mountain View, CA 94043; [o]NASA Ames Research Center, Mountain View, CA 94035; [p]Steward Observatory, University of Arizona, Tucson, AZ 85721; [q]Department of Astrophysics, American Museum of Natural History, New York, NY 10024; [r]Sibley School of Mechanical and Aerospace Engineering, Cornell University, Ithaca, NY 14853; [s]Department of Physics and Astronomy, University of Georgia, Athens, GA 30602; [t]Jet Propulsion Laboratory, California Institute of Technology, Pasadena, CA 91125; and [u]Department of Physics and Astronomy, The Johns Hopkins University, Baltimore, MD 21218

Edited by Neta A. Bahcall, Princeton University, Princeton, NJ, and approved March 27, 2014 (received for review January 30, 2014)

The Gemini Planet Imager is a dedicated facility for directly imaging and spectroscopically characterizing extrasolar planets. It combines a very high-order adaptive optics system, a diffraction-suppressing coronagraph, and an integral field spectrograph with low spectral resolution but high spatial resolution. Every aspect of the Gemini Planet Imager has been tuned for maximum sensitivity to faint planets near bright stars. During first-light observations, we achieved an estimated *H* band Strehl ratio of 0.89 and a 5-σ contrast of 10^6 at 0.75 arcseconds and 10^5 at 0.35 arcseconds. Observations of Beta Pictoris clearly detect the planet, Beta Pictoris b, in a single 60-s exposure with minimal postprocessing. Beta Pictoris b is observed at a separation of 434 ± 6 milliarcseconds (mas) and position angle 211.8 ± 0.5°. Fitting the Keplerian orbit of Beta Pic b using the new position together with previous astrometry gives a factor of 3 improvement in most parameters over previous solutions. The planet orbits at a semimajor axis of $9.0^{+0.8}_{-0.4}$ AU near the 3:2 resonance with the previously known 6-AU asteroidal belt and is aligned with the inner warped disk. The observations give a 4% probability of a transit of the planet in late 2017.

high-contrast imaging | extreme adaptive optics | debris disks

Direct imaging is a powerful complement to indirect exoplanet detection techniques. In direct imaging, the planet is spatially resolved from its star, allowing it to be independently studied. This capability opens up new regions of parameter space, including sensitivity to planets at >5 AU. It also allows spectroscopic analysis of the light emitted or reflected by the planet to determine its composition (1, 2) and astrometry to determine the full Keplerian orbital elements (3, 4).

Imaging planets is extremely challenging—Jupiter is 10^9 times fainter than our sun in reflected visible light. Younger extrasolar planets are more favorable targets. During their formation, planets are heated by the release of gravitational potential energy. Depending on the exact formation process and initial conditions, a 4-Jupiter mass (M_J) planet at an age of 10 million years could have a luminosity between 10^{-6} and $2\times10^{-5}L_\odot$ (5), but this is still a formidable contrast ratio. To overcome this, astronomers combined large telescopes (to reduce the impact of diffraction), adaptive optics (to correct for phase errors induced by atmospheric turbulence), and sophisticated image processing (6, 7). This recipe in various combinations had achieved several notable successes (8–12). However, the rate of these discoveries remains low (13–15) in part because the number of suitable young stars in the solar neighborhood is low, and for all but the closest stars, such detection is limited to >20 AU, where planets may be relatively rare. To move beyond this limited sample, dedicated instruments are needed that are designed specifically for high-contrast imaging. One such instrument is the Gemini Planet Imager (GPI). GPI is a fully optimized high-contrast AO facility deployed on an 8-m telescope and is almost an order of magnitude more sensitive than the instruments of the previous generation. With this powerful dedicated facility, large-scale surveys could increase the sample of directly imaged giant planets to 25–50 or more (16). We present an overview of the design of GPI, discuss its initial operation and performance, and show first-light science results.

Design of the Gemini Planet Imager

At high dynamic ranges, the point spread function (PSF) of a bright star imaged through a telescope is complex (17, 18), with

Significance

Direct detection—spatially resolving the light of a planet from the light of its parent star—is an important technique for characterizing exoplanets. It allows observations of giant exoplanets in locations like those in our solar system, inaccessible by other methods. The Gemini Planet Imager (GPI) is a new instrument for the Gemini South telescope. Designed and optimized only for high-contrast imaging, it incorporates advanced adaptive optics, diffraction control, a near-infrared spectrograph, and an imaging polarimeter. During first-light scientific observations in November 2013, GPI achieved contrast performance that is an order of magnitude better than conventional adaptive optics imagers.

Author contributions: B.M., J.R.G., R.D., J.D., S.G., B.R.O., D.P., L.S., and J.K.W. designed research; B.M., J.R.G., P.I., Q.K., C.M., M.P., L. Poyneer, B.B., T.B., A.S.B., A.C., J.C., R.J.D.R., D.D., R.D., J.D., D.E., M.P.F., D.G., S.G., M.H., P.H., P.K., J.L., J. Maire, F.M., M.S.M., J. McBride, M.M.-B., K.M., A.N., B.R.O., D.P., J.P., L. Pueyo, F.R., N.S., L.S., D.S., A. Serio, R.S., A. Sivaramakrishnan, I.S., S.T., J.K.W., S. Wiktorowicz, and S. Wolff performed research; J.R.G., P.I., Q.K., C.M., M.P., and L. Poyneer analyzed data; and B.M. and J.R.G. wrote the paper.

The authors declare no conflict of interest.

This article is a PNAS Direct Submission.

[1]To whom correspondence should be addressed. E-mail: bmacintosh@stanford.edu.

light scattered by a variety of different mechanisms and imperfections interacting coherently and varying on different timescales. Atmospheric turbulence induces large wavefront phase errors (and smaller intensity fluctuations). These are corrected (imperfectly) by the adaptive optics (AO) system; the residual phase errors produce a halo of scattered light. Instantaneously and monochromatically, this halo is broken up into individual speckles. Over long exposures, these speckles move randomly and the atmospheric component of the halo reduces to a smooth profile. However, if the measurements of the phase used to control the adaptive optics are biased, the residual phase will have a nonzero mean, and the speckle pattern will have persistent components that could be mistaken for a planet. These can be attenuated through PSF subtraction (6), but often the exact bias will vary as, e.g., the mean seeing changes, resulting in a halo that changes on timescales of minutes (19). Additional sources of persistent speckles are intensity variations due either to reflectivity variations or to propagation of wavefront errors on surfaces not conjugate to the deformable mirrors (DM) (20). Even in the absence of wavefront errors, the finite aperture of the telescope causes diffraction that can swamp the planetary signal.

GPI is designed to deal with these errors through multiple approaches. The AO system has a large number of degrees of freedom and operates at high cadence to minimize residual atmospheric turbulence. An apodized-pupil Lyot coronagraph (APLC) (21) removes residual diffraction. Most importantly and uniquely, the entire design of the optical system is intended to minimize biases in the wavefront measurement and in turn minimize quasi-static speckles.

The instrument was also designed to minimize the chromaticity of the PSF—the APLC design sacrifices inner working angle for achromaticity (21), the number of transmissive elements is kept to a minimum, individual mirrors are polished to <1 nm RMS surface error (in the spatial frequency bandwidth of 4–24 cycles per pupil), and optics near focal planes are avoided to reduce chromatic Fresnel effects. As a result, the residual speckle pattern is highly correlated between different wavelength channels and can be further attenuated through multiwavelength postprocessing (22). Table 1 summarizes the properties of the instrument.

Adaptive Optics and Optomechanical Systems. The adaptive optics system is intended to improve on previous facilities in two respects: lower total wavefront error from dynamic sources and lower quasi-static errors by an order of magnitude. Typical current AO systems such as the 349-actuator system on the Keck telescopes (23) have ≃250 nm RMS of dynamic wavefront error on a bright star (24); GPI is designed to achieve ≃ 90 nm. The static errors of current systems are hard to estimate but generally are 50–100 nm RMS. For the Keck AO system this number is 113 nm (25); the design goal for GPI was 10 nm.

Table 1. Properties of the Gemini Planet Imager

Property	Value
Deformable mirror	64×64 MEMS*
AO wavefront sensor	Spatially-filtered Shack-Hartmann
AOWFS format	$N = 43$ subapertures 2×2 pixels
AO limiting mag.	$I = 10$ mag
Coronagraph IWA	$2.8\lambda/D$
IFS wavelength range	1.0–2.5 μm, split in five bands
IFS spectral resolution	$\lambda/\delta\lambda = 30 - 70$, or broadband polarimetry
IFS spatial sampling	0.0143 arcseconds per pixel
IFS field of view	2.78 × 2.78 arcseconds

*1,493 active actuators.

To achieve this, GPI adopts several novel features. The high-order AO system has 43 subapertures across the Gemini South pupil. A conventional piezoelectric DM with this number of subapertures would have a diameter ≥20 cm, resulting in an instrument too large for the Cassegrain focus. Instead, GPI uses a silicon MEMS DM manufactured by Boston Micromachines Corporation (26). This DM has 64 × 64 (4,096) actuators—GPI uses a 48-actuator circle (including slaved actuator rings) within this area. This compact (25.6-mm diameter) device enables precision AO correction within a small volume and mass (2,200 kg). The MEMS DM has two noteworthy limitations. First, the total displacement range is ∼4 μm, insufficient to fully correct atmospheric turbulence. GPI therefore also employs a piezoelectric, low-order DM, referred to as a "woofer." Second, the MEMS DM has five defective actuators inside the controlled pupil. Light from these bad actuators is blocked by the coronagraphic Lyot mask. Tip/tilt control is provided jointly by a piezoelectric mount for the whole woofer DM (<30 Hz) and actuation of the woofer surface itself (>30 Hz).

GPI employs a Shack–Hartmann wavefront sensor (AOWFS). Such sensors are susceptible to aliasing of errors outside the Nyquist range, which can inject significant midfrequency wavefront errors into the final image. A spatial filter (27) was installed to mitigate this. The spatial filter is adjustable with size set by the Nyquist criterion. The spatial filter can also be used for calibration. By adjusting it to a pinhole we can inject a nearly perfect spherical wavefront into the AOWFS, allowing fast calibration of the dominant source of non–common-path aberrations in the system. GPI uses a computationally efficient Fourier transform reconstructor (28) to translate AOWFS slopes into DM commands. The control loop gain of each Fourier mode is individually optimized (29) to minimize total wavefront error as atmospheric turbulence and star brightness vary.

GPI operates at a Cassegrain focus and so is subject to a variable gravity vector. The mechanical structure of GPI is therefore designed to minimize and actively control flexure. Individual

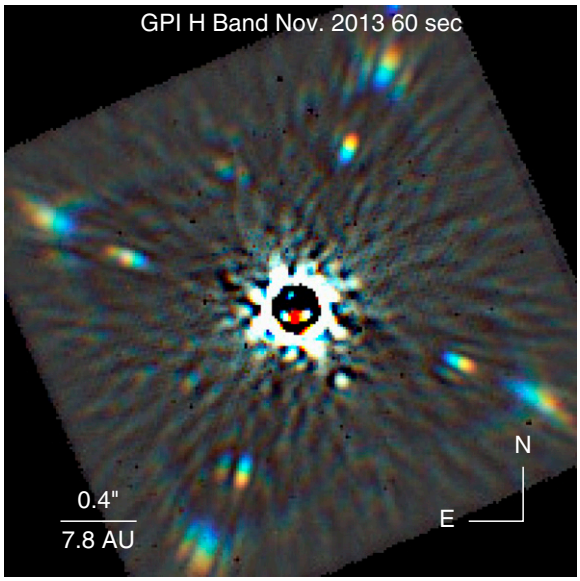

Fig. 1. RGB color composite of a single 60-s *H* band (1.5–1.8 μm) GPI image of Beta Pictoris. The short, medium, and long segments of *H* band are mapped to RGB. The image has been high-pass filtered to remove diffuse background light, but no PSF subtraction has been applied. The four sharp spots at 1:00, 4:00, 7:00, and 10:00 are diffracted images of the star generated by a reference grid inside GPI.

components such as the DM and lenslets remain optically registered to each other to within a few microns.

Coronagraph, Science Instrument, and IR Wavefront Sensor. GPI uses an APLC, which suppresses diffraction by using a gray-scale mask to taper the transmission near the edges of the pupil. The transmission profile of this mask is matched to the Fourier transform of the hard-edged focal-plane stop (radius $2.8\lambda/D$) such that residual diffraction is channeled outside the telescope pupil at a Lyot stop (21). The masks were implemented with a dithered half-tone pattern of metal dots on a glass substrate; the focal-plane stop operates in reflection as a gold-coated mirror with a small central hole. The machined Lyot stops are located inside the cryogenic spectrograph. A grid of narrow, widely spaced lines printed onto the apodizer forms a 2D grating, producing diffracted images of the central star in a square pattern. These satellite images (Fig. 1) track the star's position and intensity, facilitating astrometric and photometric calibration data (30, 31).

A near-infrared (IR) pointing and low-order wavefront sensor maintains the star in the center of the focal plane mask hole through feedback to the AO system. GPI also includes a high-accuracy near-IR interferometer integrated with the coronagraph optics to provide time-averaged measurements of the wavefront at the focal plane stop, similar to that used at Palomar (32), although this has not yet been tested on sky.

The science instrument is a near-IR integral field spectrograph (IFS) (33). Similar to the OSIRIS and P1640 instruments, it samples each spatial location in the focal plane using a lenslet array and disperses each resultant sample using a prism producing ~37,000 individual microspectra. Each spatial pixel corresponds to 0.0143 arcseconds on the sky. In a single exposure, for each location in the field of view the IFS produces a $\lambda/\delta\lambda \simeq 30-70$ spectrum over one of the standard astronomical bands (*YJHK*, with *K*-band split in two). The IFS uses a Teledyne Hawaii 2RG detector. A flexible and automated data pipeline transforms raw data into calibrated datacubes and starlight-subtracted images. This open-source software and extensive documentation is freely available.

First-Light Adaptive Optics Performance

GPI was extensively characterized at the University of California, Santa Cruz, before shipping to Chile (34). In October 2013 it was attached to the bottom Cassegrain port of the Gemini South telescope. After some brief alignment tests, first light occurred on November 12, 2013 (UT); the first testing run continued until November 18, with a second observing run from December 9 to 12.

The instrument met its initial performance goals. The AO system locked onto every target attempted, even in seeing with a Fried parameter of $r_0 \simeq 5$ cm. The AO loop closed on stars $I \leq 8$ mag. (GPI will operate down to $I \simeq 10$ mag in better seeing.) GPI can save extensive AO telemetry at the full system frame rate, including DM commands, raw wavefront sensor images and centroids, reconstructed phases, and tip/tilt measurements and commands. These have been used to generate an error budget (Table 2) for typical observations of β Pictoris ($I = 3.8$ mag.) from observations taken on December 11 (UT). The Fried parameter r_0 was estimated to be 20 cm from measurements earlier in the night with a differential image motion monitor located outside the Gemini dome, corresponding to better-than-average seeing. Most error terms are directly estimated from AO telemetry, following methods used in ref. 24.

Table 2. Adaptive optics error budget for observations of Beta Pictoris

Error term	RMS value, nm
Fitting error*	60
Servo-lag error†	50
AOWFS measurement noise†	6
Static edge excursions‡	31
Other static residuals†	13
60 Hz vibration, CCRs at full power	100
60 Hz vibration, CCRs at 50% power	30–50
Residual non-common-path§	30
Total, CCRs at full power	134
Total, CCRs at minimum power	98

*Estimated from r_0 =18 cm.
†Calculated from AOWFS residuals.
‡Calculated from average DM shape.
§Estimated from internal calibration source, mostly low frequency.

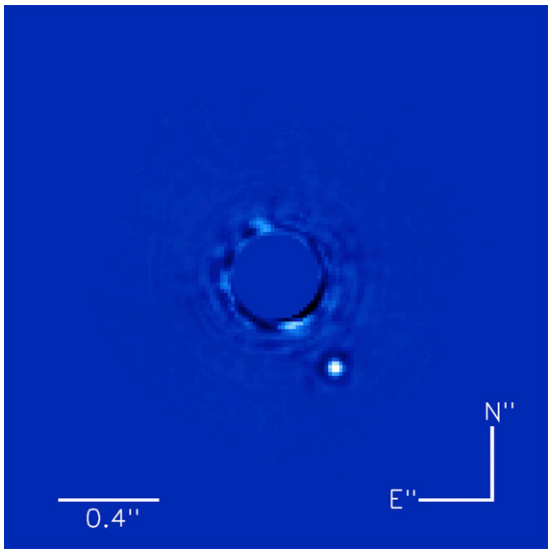

Fig. 2. Combined 30-min GPI image of Beta Pictoris. The spectral data have been median-collapsed into a synthetic broadband 1.5–1.8 μm channel. The image has been PSF subtracted using angular and spectral differential techniques. Beta Pictoris b is detected at a signal-to-noise of ~100.

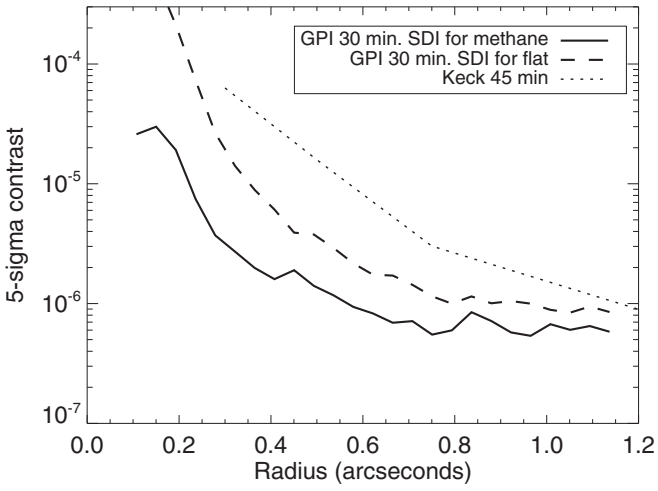

Fig. 3. Contrast vs. angular separation at *H* (1.6 μm) for a PSF-subtracted 30-min GPI exposure. Contrast is shown for PSF subtraction based on either a flat spectrum similar to a L dwarf or a methane-dominated spectrum (which allows more effective multiwavelength PSF subtraction.) For comparison, a 45-min 2.1-μm Keck sequence is also shown. (Other high-contrast AO imaging setups such as Subaru HiCIAO, Gemini NICI, and VLT NACO have similar performance to that of Keck.)

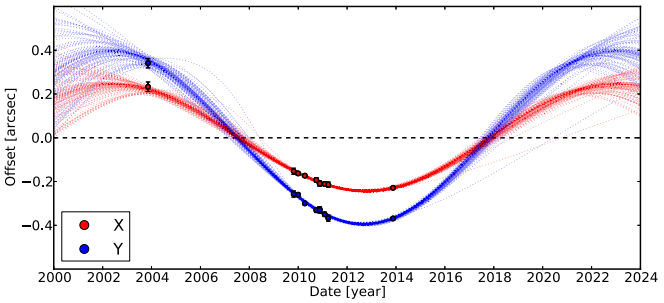

Fig. 4. The projected separation of β Pic b relative to β Pic in celestial coordinates. Data before the GPI point in late 2013 are from ref. 3. The GPI measurement shows that β Pic b has passed quadrature and allows a prediction of conjunction in September–December 2017. The red and blue trajectories show 100 solutions drawn from the posterior distribution of likely orbital solutions determined from our Monte Carlo Markov chain analysis of these data.

Two error terms are worth further discussion. The first is a quasi-static offset on the MEMS DM, consisting primarily of a phase excursion in the outer two rings of subapertures. Although this is the largest quasi-static term in the error budget, it likely has only a small effect on final images because the APLC transmission for those subapertures is low. The likely cause is a reconstruction of centroid patterns that do not correspond to a physical wavefront (such as rotation of the whole centroid pattern), and it will be mitigated through software changes. The second is a strong 60-Hz vibration. The Stirling cycle cryocoolers on GPI induce vibration at harmonics of 60 Hz in the GPI mechanical structure. Internal to GPI, these contribute about 6–8 mas of RMS tip/tilt image motion at 120 and 180 Hz, as measured with our artificial star unit. Observing actual stars through the telescope, we see an additional 10 mas of 60-Hz image motion, indicating a component external to GPI is vibrating. More significantly, there is 100 nm (time domain RSS of the spatial RMS) of low-order wavefront vibration at 60 Hz, primarily focus, when the cryocoolers are operating. This may indicate that the telescope's mirrors, which are very lightweight, are being driven by the GPI vibrations. We carried out measurements with the cryocoolers both at full power and reduced to $\simeq 30\%$ power. Modifications to the cryocoolers in January 2014 are expected to significantly reduce the vibration.

With the cryocoolers at full power, we estimate the RMS wavefront error to be 134 nm; with the cryocoolers at minimum power, the RMS wavefront error is 98 nm (exclusive of tip/tilt), corresponding to a Strehl ratio of 0.87 at 1.65 μm. Although this is very good AO performance, it is not vastly better than other high-order AO systems. However, GPI significantly exceeds the raw image contrast of such systems—we ascribe the difference to much better control of quasi-static and systematic errors.

First-Light Science: Beta Pictoris b

Here we discuss observations of β Pic. This young, nearby (19.4 pc), A6V star has a bright, edge-on debris disk (35) and a directly imaged super-Jupiter, β Pic b, orbiting at ≃10 AU (10). Various asymmetries in disk structure have been discovered (36, 37), including a midplane warp at ∼50 AU that has been attributed to a possible planetary perturbation (38–40).

Imaging and Contrast. The planet has been detected by VLT/NACO (10), Gemini/NICI (41), and the Magellan AO system (42). We observed the planet in *H* band (1.65 μm) on November 18 (2013) UT. We obtained 33 individual 60-s images in coronagraphic mode, with the cryocoolers operated at minimum power. The planet was immediately visible in a single raw 60-s exposure (Fig. 1). For comparison, a lower signal-to-noise *H*-

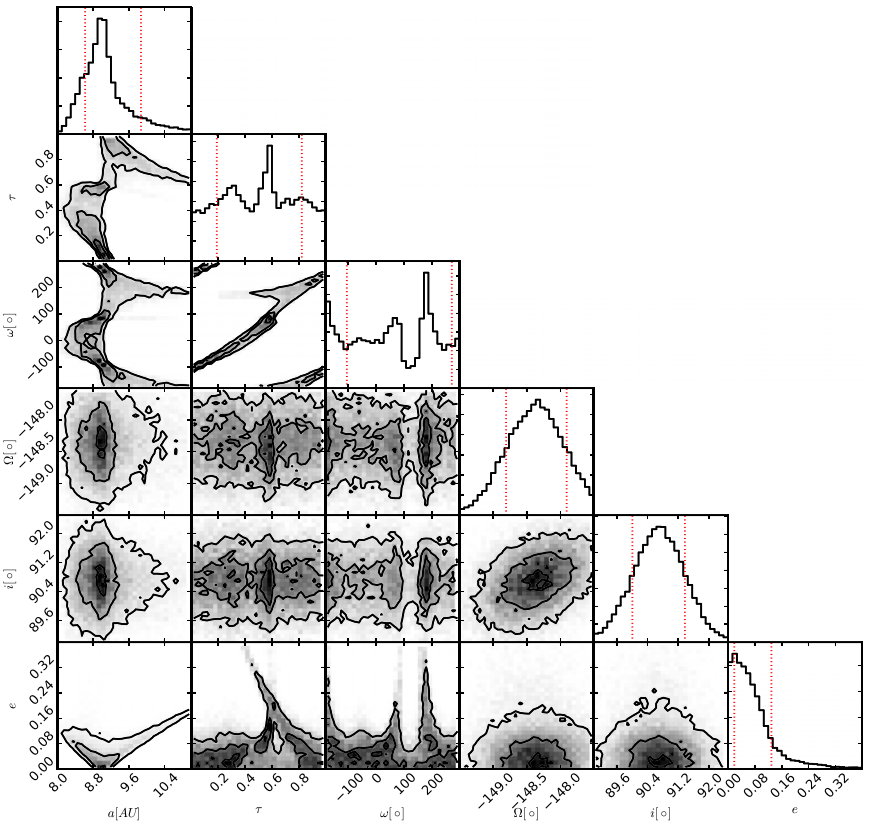

Fig. 5. Posterior distribution of the orbital elements of β Pic b: semimajor axis, *a*; epoch of periapse, τ (in units of the orbital period); argument of periapse, ω; argument of the ascending node, Ω; inclination, *i*; and eccentricity, *e*. The plot shows the joint distributions as contours (0.1, 0.5, and 0.9) and marginalized probability density functions as histograms. The well-represented degeneracy in ω, e.g., see ω versus *a*, is good evidence of reliable sampling of the posterior distribution. Vertical dotted lines in the histograms denote the 68% confidence interval.

Table 3. Orbital parameters of Beta Pictoris b

Orbital element	Value*	Units
a	$9.04^{+0.82}_{-0.41}$	AU
Ω	-148.36 ± 0.45	deg
i	90.69 ± 0.68	deg
e	$0.06^{+0.07}_{-0.04}$	
P	$20.5^{+2.9}_{-1.4}$	y
$(1-e)a$	$8.75^{+0.24}_{-0.81}$	AU
$(1+e)a$	$9.39^{+1.55}_{-0.33}$	AU

*The quoted value is the median (50th percentile) of the marginalized posterior distributions with errors representing the 68% confidence interval (16th and 84th percentiles). Derived quantities (period, *P*, and periapse and apoapse distances) are also listed.

band detection using NICI (41) required 3,962 s of exposure and extensive PSF subtraction.

A set of 30 images were PSF-subtracted using a modified version of the TLOCI algorithm (43). For each data cube wavelength slice, the remaining wavelengths, and the images at the same wavelength acquired at a different time, are used as PSF reference images. A simulated planet having either a flat spectrum similar to L-dwarfs or a CH_4-dominated spectrum similar to T-dwarfs is used to exclude reference images with more than 10% self-overlap of the planet with the image being processed. The selected reference images are then used to subtract the stellar noise by performing a LOCI least-squares fit constrained to positive coefficients. All star-subtracted data cubes are then rotated to put north up and median combined (Fig. 2).

We evaluate the contrast of the final image by calculating the SD of the intensity in concentric annuli about the star. Fig. 3 shows a plot of contrast for a 30-min set of GPI data. In 30-min exposures, GPI is performing $\sim$2 magnitudes better than typical contrast obtained at the Keck Observatory.

Astrometry. We use these images to constrain the orbit of β Pic b. Most astrometric calibrators are unsuitable for GPI because of the small field of view (2.8 arcseconds on a side) and also because for low-contrast ratio binary stars the secondary will either saturate the science detector or light from the secondary will perturb the wavefront sensor. Therefore, we calibrated the scale and orientation of GPI using other extrasolar planets as references. We compared the offset between HR 8799c and HR 8799d measured at the W. M. Keck Observatory in October 2013 with GPI observations of this system. The position of β Pic b is measured from the combined TLOCI image. The position of β Pic b is estimated in each raw 60-s image from the center of the square pattern defined by the four reference-grid spots. The measured separation of β Pic b is 434 ± 6 mas at a position angle of $211.8 \pm 0.5°$.

We fit the GPI astrometric measurements presented here together with the compilation of data in ref. 3, using Markov Chain techniques described in ref. 4. The adaptive Metropolis–Hasting sampler used in ref. 4 has been replaced by an affine invariant sampler (44, 45). Fig. 4 shows an ensemble of trajectories computed using orbital elements sampled from the joint posterior distribution. The results show a good fit.

The GPI data point implies that β Pic b has recently turned around on its orbit and roughly one half an orbital period has elapsed since the first astrometric measurement. The combination of small measurement errors and the lever arm provided by extended orbital coverage yields the best estimate to date of the semimajor axis. Our measurement places β Pic b at a semimajor axis of $9.0^{+0.8}_{-0.4}$ AU, with a corresponding period of $20.5^{+2.9}_{-1.4}$ y. Beta Pic b will remain observable (>0.2 arcseconds) at least until March 2016 and will likely reappear before October 2019. A possible transit of the planet across the star was observed in 1981 (46). Our estimated orbital inclination is $90.7 \pm 0.7°$; transits of β Pic will occur if the inclination is within 0.05° of edge on. The next opportunity to observe such a transit by β Pic b is in September through December 2017 (68% confidence).

The orbit has a small but nonzero eccentricity ($e = 0.06^{+0.07}_{-0.04}$). The corresponding range between periaspe and apoapse (8.8–9.4 AU; Table 3) falls neatly between the 6.4 AU and 16 AU asteroidal belts (47–49) and places the inner belt close to the 3:2 commensurability with the orbital period of β Pic b.

Our results agree with refs. 3 and 50. The chief difference is the improvement in the confidence intervals (Table 3). Distinct peaks are beginning to emerge in the posterior distribution for epoch of periapse and for ω (Fig. 5). Moreover, the 68% confidence interval for i drops from 3.4° to 1.36°—the planetary orbit is likely inclined to the line of sight, leaving a small chance (4%) that β Pic b transits the star. The longitude of the ascending node now has a confidence interval of 0.9° compared with 3° previously. The corresponding PA is $211.6 \pm 0.°5$ and clearly misaligned with the main disk ($PA = 209 \pm 0.°3$) but more nearly aligned with the inner warped component (3, 51).

These results show the power of a dedicated high-contrast imager; GPI achieves a given contrast ratio sensitivity $\sim$50 times faster than the best previous-generation systems. A 600-star survey of young nearby stars will begin in 2014, with the goal of producing a sample of directly imaged planets that (*i*) spans a broad range of temperatures, ages, and masses, opening up new areas of planetary atmosphere phase space, and (*ii*) probes the range of semimajor axes and stellar ages inaccessible to Doppler and transit surveys to produce statistical constraints on planet formation models. Simulations predict that this survey will discover 25–50 exoplanets (16) with masses as low as that of Jupiter and at separations as close as 3–5 AU. Using a polarimetry mode, the survey will also map debris disks. GPI will be available to the astronomical community for guest observer projects, ranging from studying young solar system objects to the outflows from evolved stars. With the advent of GPI and similar dedicated facilities, high-contrast imaging, spectroscopy, and polarimetry will open up a new segment of other solar systems to characterization.

ACKNOWLEDGMENTS. We thank the international team of engineers and scientists who worked to make GPI a reality. We especially recognize the unique contributions of Gary Sommargren, Steven Varlese, Christopher Lockwood, Russell Makidon, Murray Fletcher, and Vincent Fesquet, who passed away during the course of this project. We acknowledge financial support of the Gemini Observatory, the National Science Foundation (NSF) Center for Adaptive Optics at University of California, Santa Cruz, the NSF (AST-0909188; AST-1211562), NASA Origins (NNX11AD21G and NNX10AH31G), the University of California Office of the President (LFRP-118057), and the Dunlap Institute, University of Toronto. Portions of this work were performed under the auspices of the U.S. Department of Energy by Lawrence Livermore National Laboratory under Contract DE-AC52-07NA27344 and under contract with the California Institute of Technology Jet Propulsion Laboratory funded by NASA through the Sagan Fellowship Program executed by the NASA Exoplanet Science Institute.

1. Konopacky Q, et al. (2013) Detection of carbon monoxide and water absorption lines in an exoplanet atmosphere. *Science* 339(6126):1398–1401.
2. Oppenheimer BR, et al. (2013) Reconnaissance of the HR 8799 exosolar system. I. Near-infrared spectroscopy. *Astrophys J* 768(1):24–40.
3. Chauvin G, et al. (2012) Orbital characterization of the *β* Pictoris b giant planet. *Astron Astrophys* 542:A41.
4. Kalas P, Graham JR, Fitzgerald MP, Clampin M (2013) STIS coronagraphic imaging of Fomalhaut: Main belt structure and the orbit of Fomalhaut b. *Astrophys J* 775(1):56.
5. Marley MS, Fortney JJ, Hubickyj O, Bodenheimer P, Lissauer JJ (2007) On the luminosity of young Jupiters. *Astrophys J* 655(1):541–549.
6. Lafrenière D, Marois C, Doyon R, Nadeau D, Artigau É (2007) A new algorithm for point-spread function subtraction in high-contrast imaging: A demonstration with angular differential imaging. *Astrophys J* 660(1):770–780.
7. Soummer R, Pueyo L, Larkin J (2012) Detection and characterization of exoplanets and disks using projections on Karhunen-Loève eigenimages. *Astrophys J* 755(2): L28–L32.

8. Kalas P, et al. (2008) Optical images of an exosolar planet 25 light-years from Earth. *Science* 322(5906):1345–1348.
9. Marois C, et al. (2008) Direct imaging of multiple planets orbiting the star HR 8799. *Science* 322(5906):1348–1352.
10. Lagrange AM, et al. (2010) A giant planet imaged in the disk of the young star β Pictoris. *Science* 329(5987):57–59.
11. Rameau J, et al. (2013) Discovery of a probable 4-5 Jupiter-mass exoplanet to HD 95086 by direct imaging. *Astrophys J* 772(2):L15–L20.
12. Kuzuhara M, et al. (2013) Direct imaging of a cold Jovian exoplanet in orbit around the Sun-like star GJ 504. *Astrophys J* 774(1):11–21.
13. Biller BA, et al. (2013) The Gemini/NICI Planet-Finding Campaign: The frequency of planets around young moving group stars. *Astrophys J* 777(2):160–200.
14. Nielsen E, et al. (2013) The Gemini NICI Planet-Finding Campaign: The frequency of giant planets around young B and A stars. *Astrophys J* 776(1):4–39.
15. Wahhaj Z, et al. (2013) The Gemini Planet-Finding Campaign: The frequency of giant planets around debris disk stars. *Astrophys J* 773(2):179–209.
16. McBride J, et al. (2011) Experimental design for the Gemini Planet Imager. *Publ Astron Soc Pac* 123(904):692–708.
17. Sivaramakrishnan A, Koresko C, Makidon R, Berkefeld T, Kuchner M (2001) Ground-based coronagraphy with high-order adaptive optics. *Astrophys J* 552(1):397–408.
18. Perrin MD, Sivaramakrishnan A, Makidon RB, Oppenheimer BR, Graham JR (2003) The structure of high Strehl ratio point-spread functions. *Astrophys J* 596(1):702–712.
19. Hinkley S, et al. (2007) Temporal evolution of coronagraphic dynamic range and constraints on companions to Vega. *Astrophys J* 654(1):633–640.
20. Marois C, et al. (2008) An end-to-end polychromatic Fresnel propagation model of GPI. *SPIE Conf Ser,* 10.1117/12.789899.
21. Soummer R, Sivaramakrishnan A, Pueyo L, Macintosh B, Oppenheimer BR (2011) Apodized pupil Lyot coronagraphs for arbitrary apertures. III. Quasi-achromatic solutions. *Astrophys J* 729(2):144.
22. Marois C, et al. (2000) Efficient speckle noise attenuation in faint companion imaging. *Publ Astron Soc Pac* 112(767):91–96.
23. Wizinowich P, et al. (2000) First light adaptive optics images from the Keck II telescope: A new era of high angular resolution imagery. *Publ Astron Soc Pac* 112(769):315–319.
24. van Dam MA, et al. (2006) The W. M. Keck Observatory Laser Guide Star Adaptive Optics System: Performance characterization. *Publ Astron Soc Pac* 118(840):310–318.
25. van Dam MA, Le Mignant D, Macintosh BA (2004) Performance of the Keck Observatory adaptive-optics system. *Appl Opt* 43(29):5458–5467.
26. Cornelissen SA, Bierden PA, Bifano TG (2008) A 4096 element continuous facesheet MEMS deformable mirror for high-contrast imaging. *SPIE Conf Ser* 6306:6–17.
27. Poyneer LA, Macintosh B (2004) Spatially filtered wave-front sensor for high-order adaptive optics. *J Opt Soc Am A Opt Image Sci Vis* 21(5):810–819.
28. Poyneer LA, Gavel DT, Brase JM (2002) Fast wave-front reconstruction in large adaptive optics systems with use of the Fourier transform. *J Opt Soc Am A Opt Image Sci Vis* 19(10):2100–2111.
29. Poyneer LA, Véran JP (2005) Optimal modal Fourier-transform wavefront control. *J Opt Soc Am A Opt Image Sci Vis* 22(8):1515–1526.
30. Sivaramakrishnan A, Oppenheimer B (2006) Astrometry and photometry with coronagraphs. *Astrophys J* 647(1):620–629.
31. Marois C, Lafreniere D, Macintosh B, Doyon R (2006) Accurate astrometry and photometry of saturated and coronagraphic point spread Ffunctions. *Astrophys J* 647(1): 612–619.
32. Oppenheimer BR, et al. (2012) Project 1640: The world's first ExAO coronagraphic hyperspectral imager for comparative planetary science. *SPIE Conf Ser* 8447:20–43.
33. Chilcote JK, et al. (2012) Performance of the integral field spectrograph for the Gemini Planet Imager. *SPIE Conf Ser*, 10.1117/12.925790.
34. Macintosh BA, et al. (2012) The Gemini Planet Imager: Integration and status. *SPIE Conf Ser*, 10.1117/12.926721.
35. Smith BA, Terrile RJ (1984) A circumstellar disk around Beta pictoris. *Science* 226(4681): 1421–1424.
36. Lagage PO, Pantin E (1994) Dust depletion in the inner disk of Pictoris as a possible indicator of planets. *Nature* 369(6482):628–630.
37. Kalas P, Jewitt D (1995) Asymmetries in the Beta Pictoris dust disk. *Astrophys J* 110(2): 794–804.
38. Burrows CJ, et al. (1995) HST observations of the β Pic circumstellar disk. *Bull Am Astron Soc* 27:1329.
39. Mouillet D, et al. (1997) A planet on an inclined orbit as an explanation of the warp in the Beta Pictoris disc. *Mon Not R Astron Soc* 292:896–904.
40. Heap SR, et al. (2000) Space Telescope Imaging Spectrograph coronagraphic observations of Beta Pictoris. *Astrophys J* 539(1):435–444.
41. Boccaletti A, Lagrange AM, Bonnefoy M, Galicher R, Chauvin G (2013) Independent confirmation of β Pictoris b imaging with NICI. *Astron Astrophys* 551:L14–L17.
42. Males JR, et al. (2014) Magellan Adaptive Optics first-light observations of the exoplanet Beta Pic b. I. Direct imaging in the far-red optical with MagAO+VisAO and in the near-IR. *Astrophys J*, in press.
43. Marois C, Correia C, Véran JP, Currie T (2014) TLOCI: A fully loaded speckle killing machine. *Proc Int Astron Union* 299:48–49.
44. Goodman J, Weare J (2010) Ensemble samplers with affine invariance. *Commun Appl Math Comput Sci* 5:65–80.
45. Foreman-Mackey D, Hogg DW, Lang D, Goodman J (2013) emcee: The MCMC Hammer. *Publ Astron Soc Pac* 125:306–312.
46. Lecavelier Des Estangs A, et al. (1995) β Pictoris: Evidence of light variations. *Astron Astrophys* 229:557–562.
47. Weinberger AJ, Becklin EE, Zuckerman B (2003) The first spatially resolved mid-infrared spectroscopy of β Pictoris. *Astrophys J* 584(1):L33–L37.
48. Wahhaj Z, et al. (2003) The inner rings of β Pictoris. *Astrophys J* 584(2):L27–L31.
49. Okamoto YK, et al. (2004) An early extrasolar planetary system revealed by planetesimal belts in β Pictoris. *Nature* 431(7009):660–663.
50. Fitzgerald MP, Kalas PG, Graham JR (2009) Orbital constraints on the βPic inner planet candidate with Keck Adaptive Optics. *Astrophy J Lett* 706(2):L41–L45.
51. Lagrange AM, et al. (2012) The position of β Pictoris b position relative to the debris disk. *Astron Astrophys* 542:A40.